Light switchable surface topographies

Liu, Ling

3

Travelling Waves on Photo-Switchable Polymer Films by Rotating Polarized Light

Abstract

Nature employs travelling waves to generate propulsion of fluids, cells and organisms. This has inspired the development of responsive material systems based on different external triggers. Especially light-actuation is suitable because of its remote control and scalability, but often complex, moving light sources are required. Here, we developed a method that only requires flood exposure by a rotating polarized light source to generate transversely-propagating surface waves on azobenzene-modified liquid crystalline polymer films. We built a photomechanical computational model that accounts for the attenuation of polarized light and trans-to-cis isomerization of azobenzene. A non-uniform in-plane distribution of the liquid crystal molecules allows for the generation of travelling surface waves whose amplitude, speed and direction can be controlled through the intensity, direction and speed of the rotating polarized light source. Our method opens new avenues for motion control based on light-responsive topographical transformations for application in microfluidic lab-on-chip systems and soft robotics.

Keywords: Liquid crystal polymers, azobenzenes, light driven systems, topographical changes, travelling wave.

3.1 Introduction

Swimming and fluid propulsion in nature occurs predominantly by the generation of traveling waves, such as the peristalsis of annelids and the human intestines, the swimming of fish, spermatozoa and synechococcus, and the metachronal waves of ciliates. These are based on the generation of periodic travelling waves, which requires a triggering of distributed and spontaneous deformations in a coordinated

This chapter is based on the manuscript:
L. Liu, D. J. Broer, and P. R. Onck. Travelling Waves on Photo-Switchable Polymer Films by Rotating Polarized Light, submitted.

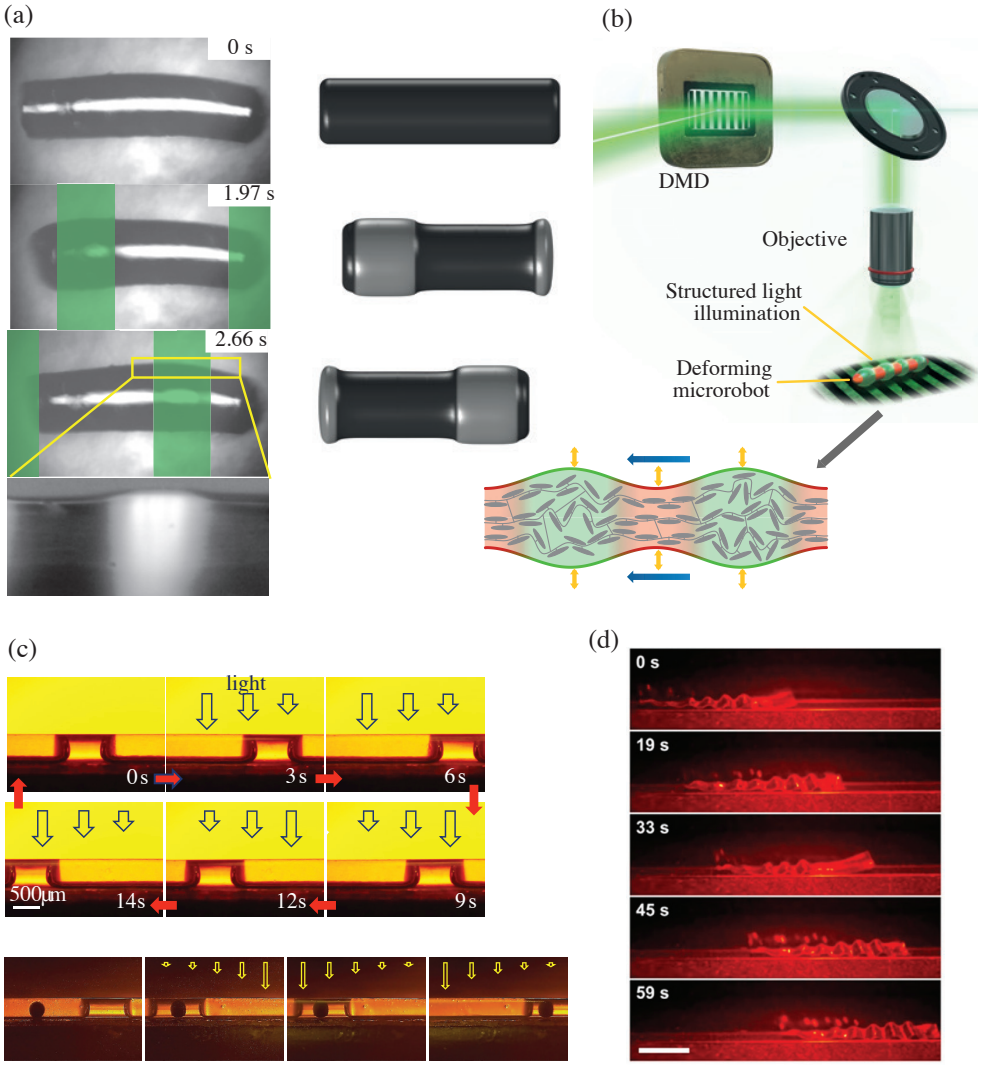

Figure 3.1 – *Experimentally realized travelling wave systems. (a)-(b) Self-swimming microrobotics. Localized exposure triggers local expansion (a) and a scanning of the structured light pattern (via a complex mirror array, (b)) initiates a travelling wave, pumping the robot. (c) Fluid and cargo transportation using travelling waves inside a tubular structure. (d) Locomotion via travelling waves. (Figures (a)-(b) reproduced from Ref. [215], (c) from [149], copyright NPG; Figure (d) from [328], copyright Wiley).*

way for mimicking such a propulsion behaviour in artificial robots [173, 215, 324–327]. This has formed the inspiration for many man-made propulsive systems for different applications, e.g., cargo transportation [329], fluid propulsion [58, 65, 274], autonomous swimming [215, 327, 330–333] and caterpillar locomotion [173, 328, 334], based on a

range of material systems, such as, gels [329, 335], elastomers [327], magnets [330], metal nanowires [332] and liquid crystal polymers [173, 215, 274, 328, 334, 336], in response to various external triggers, like electric [337, 338], heating [329, 334], magnetic [58, 330, 332] and light stimuli [173, 215, 274, 328, 331]. See Fig. 3.1 for several functionalized examples from the literature, including a light-guided self-swimming robots (a)-(b), light-triggered fluid plug movement and cargo transportation (c) and a light-controlled crawler (d). By taking advantage of its remote, scalable and precise spatial-temporal control, light often is the most appropriate actuation source and comparing favorably with electrical, magnetic and thermal actuation. However, the currently-available systems require complex matrix-like structured lenses, masks and mirrors and often requires a moving light source [184, 215, 274, 328, 331, 339]. In the chapter, we demonstrate that travelling waves can be generated under uniform light exposure by a rotating polarized light source, representing a drastic reduction in complexity.

We use liquid crystal (LC) polymeric networks, with embedded photo-responsive azobenzene chromophores, that undergo dimensional changes in response to ultraviolet (UV) light [18, 34, 67, 147, 165, 202, 275, 340]. The azobenzene molecules are cross-linked to the polymer skeleton and upon UV exposure transition from a rod-like *trans* state to a bent-like *cis* state (see Fig. 3.2(a) and (b)). This process decreases the orientational order of the neighbouring liquid crystal molecules, leading to an anisotropic mechanical response: a contraction along the average direction of the LC molecules (denoted by the director $\overrightarrow{n}$) together with an expansion in the plane perpendicular to the director. Based on this mechanism, we have developed various surface topographical transformations that are reversibly controlled by light for substrate-constrained glassy LC films [33, 34, 153]. The high-resolution imprinting of the internal molecular order using photo-alignment command layers provides the possibility to design complex director distributions and material anisotropies [28, 154, 265], and allows for miniaturization into the micrometer regime [18, 67, 301].

In this work, we use a recently-developed optomechanical model [34] to design travelling surface waves under a continuous and polarized light source that rotates in time. The spatial selectivity on actuation in the literature was achieved in a more complex way, by, e.g., scanning [215, 274, 329, 334] or oscillating or rotating [331, 332, 341] the external stimulus fields, self-shadowing [173], localized actuation [342], internal circuits [327], chemical reaction waves [335, 343] or non-uniformity of the material [328, 330]. However, only uniform flood illumination is needed here, which represents an important reduction in complexity compared to existing set-ups that rely on the use of matrix-like structured lenses, masks and mirrors, and switching-on-off as well as moving light sources [184, 215, 274, 328, 331, 339]. We take advantage of the selective absorption of the azobenzenes when oriented parallel to the electric field of the polarized light [113, 165, 176, 212, 286]. As schematically shown in Fig. 3.2(c) and (d), the directors are all confined in the plane parallel to the substrate and have a continuous rotation (relative to the x axis, see Fig. 3.2(d) as one moves in the x-direction). When the film is exposed to a polarized light source, different regions have different *trans*-to-*cis* conversion levels due to the fact that level of isomerization depends on the angle between the local director and the electric field, $\overrightarrow{E}$, of the polarized light. As a result, a periodic distribution of the *cis* concentration can be generated in the plane of the film and thus a surface protrusion is formed. Upon rotation of the electric field

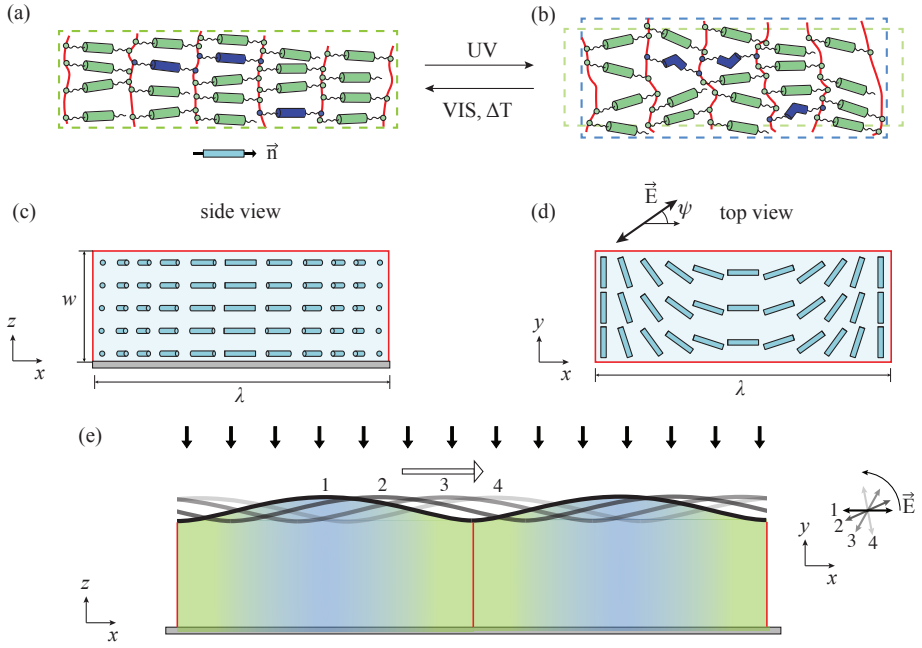

Figure 3.2 – *Schematics illustrating the set-up and the generation of travelling waves. (a)-(b) The mechanism of photo-induced deformation of azobenzene-modified liquid crystal polymers. Illumination of UV light triggers isomerization of the embedded azobenzenes (blue) from the rod-like trans state to the bent-like cis state, leading to a decrease of the orientational order of the neighbouring LC molecules (green). This process results in a contraction along the director* $\overrightarrow{n}$ *(i.e., the average direction of the LC molecules) accompanied by an expansion in the plane perpendicular to the director. (c) Side view and (d) top view of the director distribution of a unit cell, in which the director gradually rotates over 180° in one period* λ *along the* x *axis. The director distribution is uniform through the thickness and along the* y *axis. The film is actuated by a polarized light source rotating in the* x*-*y *plane (*$\overrightarrow{E}$ *denotes the electric field which makes an angle,* ψ*, with the* x *axis). (e) The generation of a travelling wave due to rotating polarized light in two neighbouring unit-cells (red lines). The wave is travelling in the direction of the large horizontal arrow and is depicted by four consecutive snapshots in time, each corresponding to a specific orientation of the electric field in the plane (right). Snapshot 1 corresponds to the situation in (c) and (d) for* $\psi = 0°$*. The blue color in the film at snapshot 1 denotes large out-of-plane expansions (a higher level of trans-to-cis isomerization) and the green color denotes low deformations.*

inside the x-y plane, a continuous change of the *cis* concentration field ensues and thus the deformation gradient guided by the polarized light leads to a travelling wave (see Fig. 3.2(e)). The propagating direction and speed of the wave can be tuned by inverting the rotation direction of the polarized light and by changing the rotation speed, respectively.

The chapter is organized as follows. The light attenuation model and the constitutive relation are discussed in section 3.2, in which the mechanism to generate a travelling surface wave is illustrated. The detailed implementation of our model in thin and thick film scenarios are addressed in section 3.3.2 and 3.3.3, respectively. The chapter concludes in section 3.4 with a discussion and conclusions.

3.2 Numerical method

3.2.1 Light attenuation model

The light attenuation model developed in Section 2.2.2 from Chapter 2 is adopted here. Please refer to that section for details.

The polarization coefficient, ζ, used in equations (2.6)-(2.7) is re-defined for polarized light illumination as [295]

$$\zeta = \frac{1}{3}\left[2SP_2(\cos\phi) + 1\right]. \tag{3.1}$$

The function $P_2(x)$ is the second Legendre polynomial defined as $P_2(x) = (3x^2 - 1)/2$ and ϕ is the angle between the local director $\overrightarrow{\mathrm{n}}$ and the electric field of the incoming light $\overrightarrow{\mathrm{E}}$. The S is the order parameter, describing the average orientational order of the local liquid crystal molecules with respect to the director $\overrightarrow{\mathrm{n}}$ [147]. If the electric field is parallel to the director, $\overrightarrow{\mathrm{E}} \parallel \overrightarrow{\mathrm{n}}$, the polarization coefficient ζ equals 1 when the order parameter $S = 1$, indicating the embedded azobenzenes, which follow the orientational order of the LC molecules, can fully absorb the UV light and thus the isomerization is maximized. On the other hand, if $\overrightarrow{\mathrm{E}} \perp \overrightarrow{\mathrm{n}}$, the probability of the azobenzenes to undergo isomerization is low (i.e., $\zeta = 0$) since the electric field is perpendicular to the long-axis of the azobenzenes, leading to a minimal effective absorption. Typical values of the order parameter S of nematic glassy liquid crystal networks range from 0.5 to 0.8 [147, 156, 299]. Here, we use $S = 0.8$, a constant value for the order parameter, thus neglecting the order decrease during the opto-mechanical deformation since the loss of order in heavily-crosslinked glassy LC polymers is usually found to be small [34, 113, 147, 287].

The time needed to reach an equilibrium (photo-stationary) state for the deformation is observed to be fast for glassy LC polymers, typically in the range of a few seconds [32–34, 159, 173, 175]. Here we assume this time to be smaller than the period of rotation of the polarized light [212], so that we only focus on the photo-stationary state. See equations (2.10)-(2.12) for details.

The values of the dimensionless light coefficients α and β depend on the wavelength and scale with the intensity of the incoming light, $\mathcal{I}_0$. The attenuation lengths, d_t and d_c, are dependent on the concentration of the azobenzene as well as the wavelength of the light source. These parameters can be obtained by fitting the results of the light attenuation equations to the measured transmitted intensities through a reference sample (see our previous work [34]), resulting in excellent agreement with experimental data. In the current study, however, we explore their effect on the generation of travelling waves. The attenuation length d_t is inversely correlated to the concentration of the azobenzene added to the LC polymer and falls typically in the range from submicrometers for heavily-dozed polymers [165] to a few micrometers [34, 158, 340] and a

few tens of micrometers [287] for systems with relatively low azo-dosages. Typical thicknesses of LC films are in the range from a few to tens of micrometers [147, 161]. Here, we fix d_t to 1 μm and vary the thickness of the film w. The quantum efficiency ratio η is taken to be equal to 3 [156, 287]. We vary the light input intensity α and keep $\alpha/\beta = 10$, which fixes d_c through Eq. (2.9).

It should be noted that the polarization can change when the light travels through the film due to the birefringence effect of the liquid crystal. This is not the case when the electric field is parallel or perpendicular to the director, but it will develop in intermediate cases where the polarization changes cyclically from a linear, to elliptical to orthogonal linear. As a result, the actual through-thickness distribution of n_c will be affected for these intermediate cases. In the current chapter, however, these effects are not accounted for. Equation (3.1) is used to capture the general probability of the UV light absorption by the embedded azobenzenes. In a similar experimental implementation [212], in which the uniaxially-aligned liquid crystal film is exposed to rotating polarized light, the surface features a continuously undulatory height change.

3.2.2 Optomechanical equations

The solution of the opto-physics model is incorporated into a constitutive relation in a description of the mechanical response owing to the UV-triggered isomerization. Please refer to section 2.2.1 for details.

The photo-Poisson ratio, $\mu^{ph} = -P_{22}/P_{11}$, is reported to range from 0.3 to 2 in various glassy polymer systems [152, 174, 183]. Some empirical values were used in previous theoretical studies (e.g., 0.4 [159], 0.7 [285] and 1 [344]). Here we take $P_{11} = -0.2$ from Ref. [34] and set $P_{22} = P_{33} = 0.2$ corresponding to a photo-Poisson ratio $\mu^{ph} = 1$.

In this study, periodic boundary conditions are employed on the lateral surfaces of the unit cell (see the red box in Fig. 3.2), in which the director rotates a full 180° in a span of λ. All displacements at the bottom surface are zero due to the rigid substrate and the top surface is traction free. The above framework is implemented numerically in the commercially available package Abaqus/Standard [298].

3.2.3 Roughness parameters

Roughness parameters are introduced to quantify the surface waves. We take the discretized point set of the top surface before the light exposure to be defined by the points (i, j) with coordinates $(x(i, j), y(i, j), z_0)$, where $i = 1, 2, ...M$, $j = 1, 2, ...N$ and $z_0 = w$. Upon actuation, the points undergo the displacements $(u_x(i, j), u_y(i, j), u_z(i, j))$. The first roughness parameter used here is the Modulation depth [153, 217], defined as the vertical distance between the highest and lowest points along the surface profile,

$$\text{modulation} = \max_{(i,j)}(u_z(i, j)) - \min_{(i,j)}(u_z(i, j)). \tag{3.2}$$

The Modulation depth only concerns the surface height change along the z axis.

We also adopt a roughness parameter that is able to incorporate the slope of the different profiles. Here, the Root Mean Square (RMS) Gradient [304], S_{dq}, is employed

to characterize the slope of the corrugated surfaces,

$$S_{\mathrm{dq}} = \sqrt{\frac{1}{(M-1)(N-1)} \sum_{i=1}^{M-1} \sum_{j=1}^{N-1} \left(\frac{u_z(i+1,j) - u_z(i,j)}{\mathrm{d}x_i} \right)^2}, \tag{3.3}$$

where $\mathrm{d}x_i = x(i+1,j) - x(i,j)$.

To analyze the applicability of the controllable travelling-wave developed here, we focus on the swimming speed V of a free-standing sheet featuring travelling waves with a speed of $U = \lambda f$ on its surface [215, 330, 345], or the propulsion speed V of fluid through a channel whose surfaces generate a peristaltic wave [346–348], to be

$$V \sim \frac{A^2 f}{\lambda}.$$

A is the wave amplitude, f is the frequency and λ represents the wavelength of deformation. In our system, the wavelength is determined by the length of the unit-cell, i.e., $\lambda = \lambda$, and the amplitude is half the Modulation, $A = 1/2 \times$ Modulation. A^2/λ is used as an indicator relevant for the propulsion ability of autonomous swimming and peristaltic pumping.

3.3 Results

3.3.1 Optimal wave amplitude at small and large film thicknesses

Under the illumination of a polarized light source, different regions absorb the incoming UV light differently due to the non-uniform director distribution resulting in varying angles ϕ between the local director and the electric field of the light $\overrightarrow{\mathrm{E}}$. As given by the opto-mechanical constitutive equation (see Eq. (2.4)), the *cis* volume fraction determines the photo-induced spontaneous deformation.

Figure 3.3(a) and (b) show the n_{c} distribution and the normalized light intensity through the film depth for two combinations of the dimensionless light parameters α and β with $\alpha/\beta = 10$ for various angles ϕ. The larger α and β values, which correspond to larger input intensities, feature a higher *trans*-to-*cis* conversion level as expected. For both intensity levels, the *cis* generation is highest at the top surface when $\overrightarrow{\mathrm{E}} \parallel \overrightarrow{\mathrm{n}}$ ($\phi = 0°$). For $\phi = 0°$, the light intensity is heavily attenuated (see Fig. 3.3(b)) leading to a sharp drop in *cis* fraction n_{c} (Fig. 3.3(a)). For larger values of ϕ the light is less strongly absorbed so that it can penetrate deeper, leading to a more uniform distribution of the *cis* concentration with increasing ϕ (Fig. 3.3(a)). Note that for the extreme case $\phi = 90°$, when $\overrightarrow{\mathrm{n}} \perp \overrightarrow{\mathrm{E}}$, the polarization coefficient ζ (see Eq. (3.1)) is minimal but not zero, since the azobenzene molecules are not perfectly aligned with the director (order parameter $S = 0.8$), so that still light is attenuated.

Next we ask the question which combination of incoming light intensity α and film thickness w should be selected for optimal wave amplitudes. These optimal amplitudes are generated when the average through thickness strain for $\phi = 0°$ is maximally different from that at $\phi = 90°$. To quantify this, we define Δn_{c} to be the

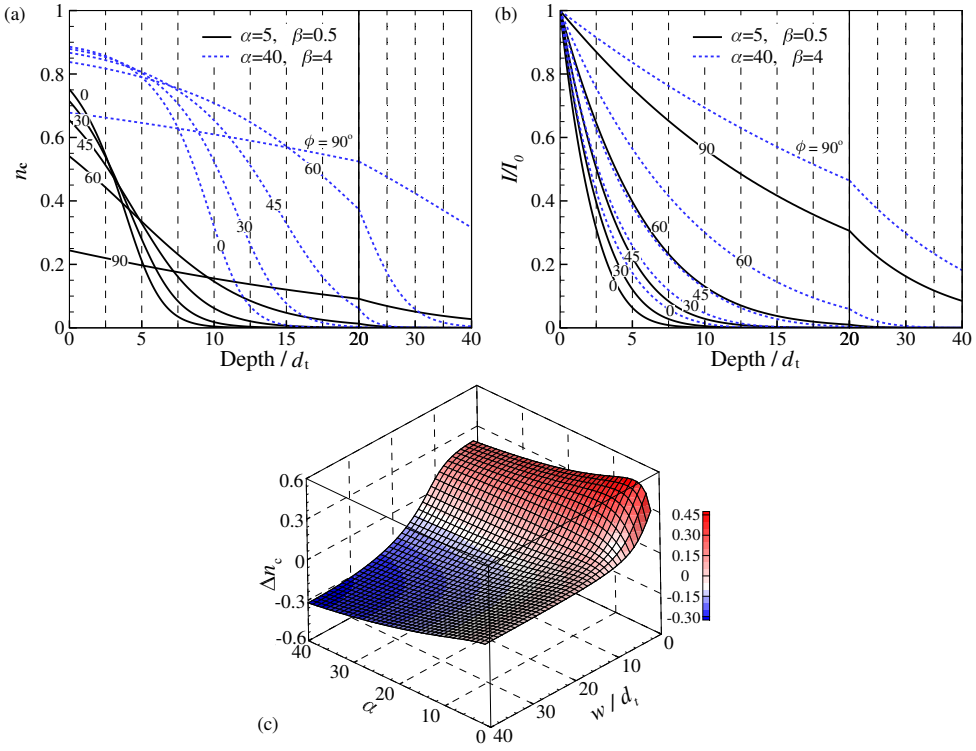

Figure 3.3 – *Light attenuation as a function of input intensity, polarization angle and film depth. The volume fraction of the cis-state azobenzene n_c (a) and the reduced light intensity $\mathcal{I} = I/I_0$ (b) against the propagating depth, normalized by the attenuation length of the trans azobenzene d_t for large ($\alpha = 40$ and $\beta = 4$) and small ($\alpha = 5$ and $\beta = 0.5$) intensities and for various angles ϕ. (c) Variation in Δn_c as a function of α and normalized film thickness w/d_t at constant $\alpha/\beta = 10$.*

difference in the *cis* volume fraction averaged through the thickness between $\overrightarrow{E} \parallel \overrightarrow{n}$ and $\overrightarrow{E} \perp \overrightarrow{n}$,

$$\Delta n_c = \frac{1}{w}\int_0^w n_c(z)|_{\phi=0^\circ} dz - \frac{1}{w}\int_0^w n_c(z)|_{\phi=90^\circ} dz.$$

Figure 3.3(c) shows the variation of Δn_c as a function of α and w/d_t. For positive values of Δn_c, the maximum ($\Delta n_c = 0.45$) occurs at $\alpha \approx 5$ for thin films, which can be verified from Fig. 3.3(a). For this situation, the region where the director is parallel to the electric field has a higher *cis* conversion level, leading to surface protrusions at the $\phi = 0^\circ$ regions. For negative values of Δn_c, however, the situation is notably different. Here the maximum Δn_c occurs at high intensities and thick films, which can be understood from the $\alpha = 40$ case in Fig. 3.3(a). For that situation the *cis* distribution through the thickness for $\phi = 90^\circ$ is much more uniform than for $\phi = 0^\circ$, leading to larger integrated n_c levels and thus to surface protrusions at the $\phi = 90^\circ$ regions.

Two distinct scenarios are explored in this work to illustrate the generation of travelling-wave-like topographical transformations controlled by rotating polarized light: thin films at a low level of input intensity and thick films at high intensity.

3.3.2 Thin films at low light intensity

Based on the maximum shown in Fig. 3.3(c), we select a light intensity of $\alpha = 5$ and $\beta = 0.5$ and a thickness of $w = 2d_t$. As shown in our previous work, the characteristic in-plane dimension relative to the film thickness is crucial for the surface topography of LC films with non-uniform director distributions [34, 217] and determines the mechanical interactions between the neighbouring regions with different director alignments. We start the analysis by taking the length of the unit cell λ (see Fig. 3.2(c)-(d)) to be 4 times the thickness, i.e., $\lambda/w = 4$. The top surface of the original film is assumed to be perfectly flat. Although we did not consider it here, possible minor surface reliefs during the photo-polymerization process due to the Marangoni effect [33, 34] can be readily incorporated.

When the film is exposed to the polarized light, gradients in the *cis* volume fractions are formed both through the thickness and along the in-plane dimension (the x axis), see Fig. 3.4(a). Upon rotation of the polarized light, the locations of the maximal and minimal *cis* concentration change along the x-axis according to the electric field orientation, $\psi = 0°$, $30°$, $60°$ and $90°$ (Fig. 3.4(a)). The prediction of the resulting topographical transformations are shown in Fig. 3.4(b) for various ψ in the range from $0°$ to $180°$ (half a period of the rotating polarized field), during which the surface wave travels one wavelength λ. All the regions undergo expansion (the horizontal axis presents the original surface), due to the non-zero *cis* fraction everywhere and due to the fact that all the directors are in the x-y plane. For the situation with $\psi = 0°$, a surface protrusion is formed at the central region, in accordance with the *cis* generation in Fig. 3.4(a). Upon rotation of the polarized light, the peak of the protrusion moves in a direction that is guided by the rotation direction of the light and the distribution of the director in the plane of the film (Fig. 3.2(d)). As a result, the protrusion moves to the right under anti-clockwise rotation of the light in the plane of the film, see Fig. 3.2(e). Note that a reversal of the rotation direction of the polarized light results in a reversal of the travelling wave direction, featuring great flexibility for a range of practical applications.

The amplitude of the surface wave is slightly changing during the movement. The red and blue open circles in Fig. 3.4(b) record the highest and lowest points, respectively, at every x-position along the film during one cycle (ψ ranging from $0°$ to $180°$ with an increment $\mathrm{d}\psi = 5°$). The wave amplitude is largest for $\psi = 0°$ and smallest for $\psi = 90°$ (see the red and blue circles in Fig. 3.4(b)). This is due to the anisotropy of the stiffness tensor. Another observation is that the specific surface profile is a function of the polarization angle ψ, see Fig. 3.4(c), with the peaks for $\psi = 90°$ being wider than for $\psi = 0°$. This effect is also reflected by the non-uniform distribution of the red circles.

In order to quantify these surface profiles and how they change with ψ, we introduce two roughness parameters: the Modulation and the Root Mean Square (RMS) gradient, S_{dq}. The Modulation is defined as the vertical distance between the highest and lowest points along the surface profile and the S_{dq} is a measure of the slope of

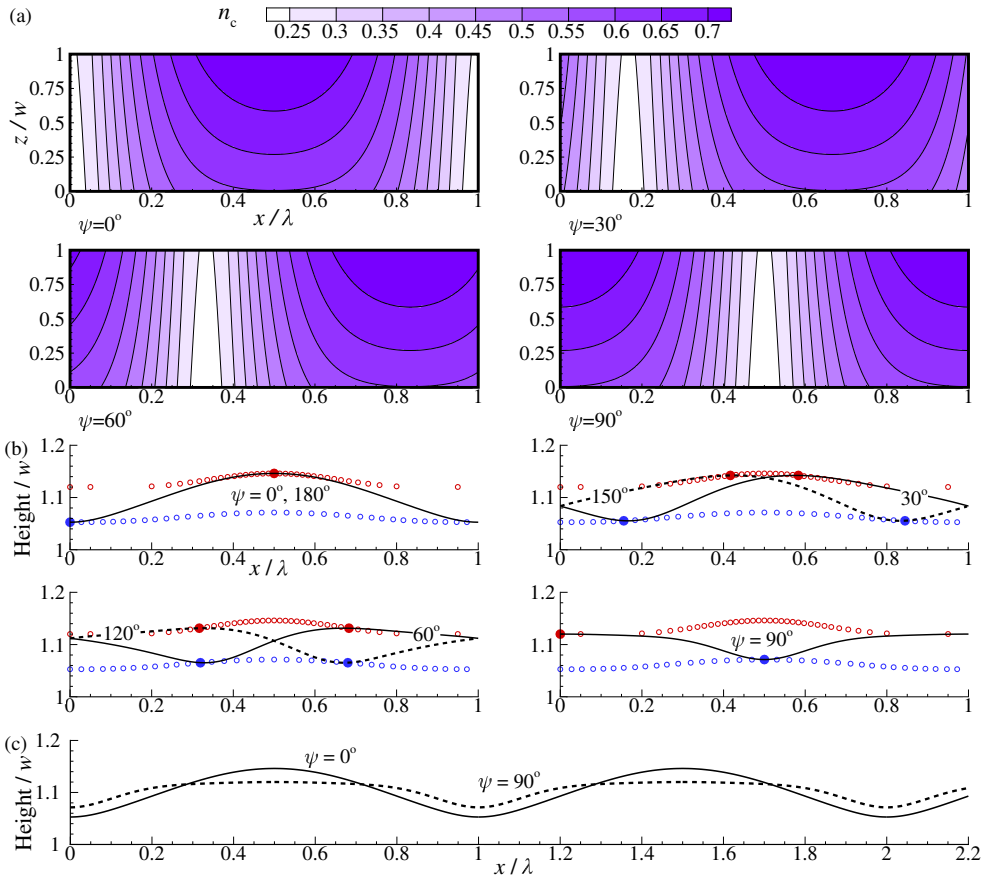

Figure 3.4 – *(a) Evolution of the trans-to-cis conversion under a rotating polarized light source at four different electric field directions: $\psi = 0°$, 30°, 60° and 90° for a thickness $w/d_t = 2$, light intensity $\alpha = 5$ and $\beta = 0.5$ and RVE size $\lambda/w = 4$. (b) The normalized surface profiles under various ψ. The red and blue open circles record the highest and lowest points for each tested electric field direction. (c) Two snapshots of the wave profile for $\psi = 0°$ (solid line) and $\psi = 90°$ (dash line). The waves are two unit cells long and the $\psi = 90°$ curve is shifted over a distance $\lambda/2$.*

the profiles (see the section 3.2.3 for their exact definition).

Figure 3.5(a) plots the variation of the Modulation, normalized by the thickness, and the S_{dq} as a function of the electric field direction, ψ. Both roughness parameters follow the same trend, reaching the highest value when the central part of the unit cell (see Fig. 3.2(d)) is most strongly actuated ($\psi = 0°$) and the lowest value when the electric field is rotated by 90° ($\psi = 90°$).

Next we study the effect of the in-plane dimension, λ. Simulations were conducted with a fixed thickness $w = 2d_t$ and a varying λ, showing that the Modulation increases and the S_{dq} decreases with increasing λ, until it reaches a ψ-independent roughness

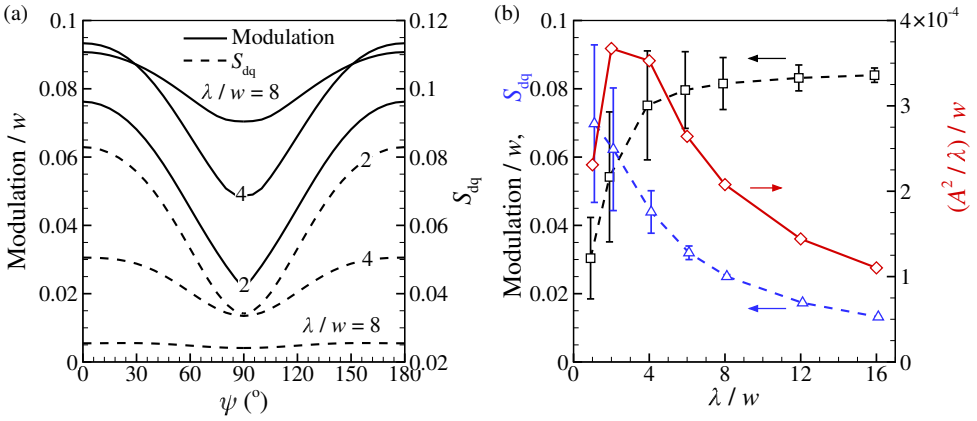

Figure 3.5 – *Variations of the Modulation normalized by the thickness and the RMS slope S_{dq} against (a) the electric field direction of the polarized light, ψ, with $\lambda/w = 2$, 4 and 8 and (b) against the dimensionless number λ/w. The film thickness and light intensity are $w/d_t = 2$ and (α, β)=(5, 0.5), respectively. The error bars in (b) indicate the standard deviation of the roughness parameters in the range of $0° \leq \psi \leq 180°$ as shown in (a). The variation of A^2/λ normalized by w as a function of λ/w is shown in (b) based on the averaged Modulations.*

profile at large λ-values (see Fig. 3.5(a) and Fig. 3.6). Since the roughness parameters themselves are dependent on the electric field direction, the average values are plotted in Fig. 3.5(b) with the corresponding error bars representing the standard deviation of the roughness parameters in the range $0° \leq \psi \leq 180°$. Consistent with Fig. 3.5(a), the normalized Modulation increases with λ/w until it reaches a plateau of 0.08 for $\lambda/w \geq 8$. For small in-plane dimensions, the mechanical interactions between different regions are strong due to the large gradient in director orientations and the anisotropy in the photo-induced strains and the elastic constants. The ψ-dependent standard deviation of the Modulation is largest for the intermediate in-plane sizes (i.e., $2 \leq \lambda/w \leq 4$) and decreases with a further increase of λ/w beyond 4 in Fig. 3.5(b). Figure 3.6 plots the evolution of the normalized surface profiles for $\lambda/w = 16$. The effect of the mechanical interaction is much lower than for $\lambda/w = 4$ so that at $\psi = 90°$ the surface profile is similar to that at $\psi = 0°$, leading to the highest averaged Modulation featuring a small variation (Fig. 3.5(b)). Thus, for larger λ/w, the amplitude of the surface wave is stable under the rotation of the polarized light, mimicking a peristaltic wave that moves at a constant velocity [349].

In contrast to the Modulation, S_{dq} decreases with increasing λ/w, due to the fact that the slope considers both the height change and the in-plane dimensions of the surface profiles. An increase of λ both increases the out-of-plane expansion (due to the relaxed mechanical constraints) as well as the in-plane dimensions, the competition of which results in a decreasing S_{dq}. The ψ-dependent standard deviation of S_{dq} is observed to continuously decrease with λ/w.

In order to illustrate the applicability of the travelling-surface-wave developed here for practical applications, such as, free-standing swimming [215] and peristaltic fluid

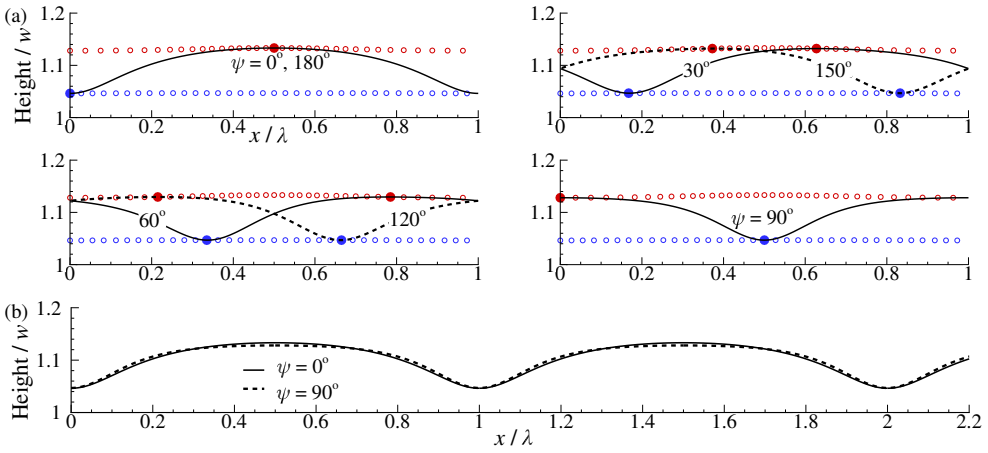

Figure 3.6 – *(a) The normalized surface profiles for various ψ for a film with a wavelength $\lambda/w = 16$, thickness $w = 2d_t$ and light intensity $(\alpha, \beta) = (5, 0.5)$. (b) Two snapshots of the wave profile for $\psi = 0°$ (solid line) and 90° (dashed line, shifted by $\lambda/2$). Due to the much lower mechanical constraints, the surface transformation resembles a peristaltic travelling wave with an almost constant amplitude. The trans-to-cis conversion status is identical to Fig. 3.4(a).*

propulsion in microchannels [345, 350], we introduce a Taylor index, A^2/λ, with A the wave amplitude and λ the wavelength which is equal to λ in our case. Figure. 3.5(b) shows the Taylor index normalized by w, as a function of λ/w. We found that it first increases when $\lambda < 2$, then reaches a maximal value in the range $2 \leq \lambda \leq 4$, which is followed by a sharp decrease for $\lambda > 4$. The results clearly show that the Taylor index is a multiplication of the Modulation and the S_{dq} value, reaching an optimal free-swimming speed or fluid-propulsion velocity for an intermediate ratio between the in-plane dimension and thickness in the range between 2 and 4.

3.3.3 Thick films

As illustrated in Fig. 3.3, in addition to the positive Δn_c achieved using a low input intensity and a small thickness, one also can explore the negative Δn_c regime using a large film thickness and a high intensity. An expanded study of the dependence of Δn_c on w/d_t and α is shown in Fig. 3.7(a), in which the regime with $\Delta n_c < -0.3$ is highlighted by the blue contour plot. There is a trench (yellow dots) depicting the a minimal Δn_c. In contrast to the maximal positive Δn_c of 0.45 for the thin film scenario, the minimal negative Δn_c is continuously decreasing for increasing α and w/d_t, even beyond the range shown in Fig. 3.7(a).

We take $w/d_t = 40$, $\alpha = 40$ and $\beta = 4$ to demonstrate wave propagation for the thick film regime. The in-plane wavelength is selected to be $\lambda/w = 4$ to allow a direct comparison with Fig. 3.4. The evolution of the *cis* generation is shown in Fig. 3.8(a) for $\psi = 0°$, 30°, 60° and 90°. A large portion of the film remains fully in the *trans* ($n_c = 0$) and passive state, since the incoming light is strongly attenuated for these thick films, especially in regions with small ϕ values (see Fig. 3.3(a) and (b)). The

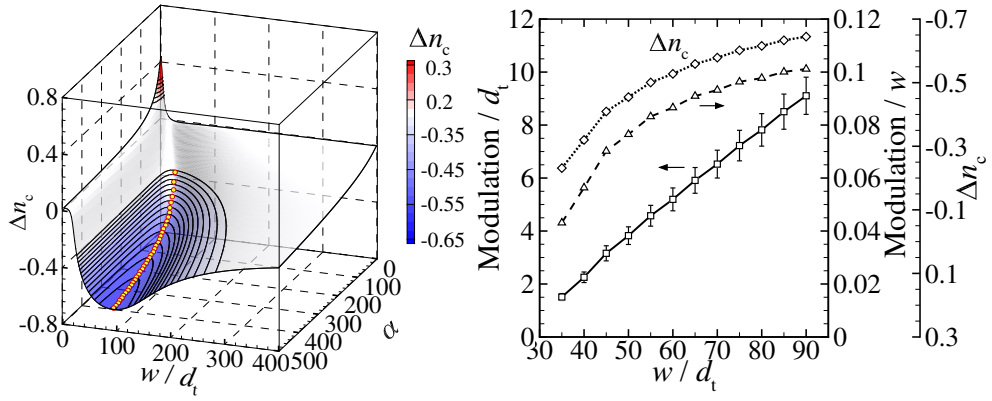

Figure 3.7 – *(a) Selection of the thickness and the light input intensity for the thick film scenario with $\lambda/w = 4$. The yellow dots indicate a trajectory of minimal Δn_c cases. (b) The Modulation normalized by the attenuation length d_t and the thickness, as well as Δn_c of the yellow dots in (a). Note that the axis of n_c is reversed. Only the error bars of the* Modulation$/d_t$ *are given for clarity.*

only exception is the region where the director is more-or-less perpendicular to the electric field $80° < \phi < 90°$). In these regions, the *cis* conversion level at the surface of the film is lower than in other regions, but the attenuation is much lower, resulting in a further penetration of the light, resulting in larger uniform *cis* levels through the thickness. The surface profile evolution is plotted in Fig. 3.8(b). Here, a striking difference is observed with the travelling wave on the thin films (Fig. 3.4(b)). In Fig. 3.8, an input with $\psi = 0°$ results in the largest expansion at $x/\lambda = 0$ and 1 for the thick films scheme where $\phi = 90°$, while for the thin films this occurs at the center ($x/\lambda = 0.5$) where $\phi = 0°$. The total out-of-plane deformation of the thick film is smaller, despite the increased light input energy, which is attributed to the large film thickness resulting in broad passive regions (Fig. 3.8(a)). In addition, the normalized wave amplitude is smaller than that of the thin films, due to the fact that $\Delta n_c = -0.32$ in Fig. 3.8 and $+0.45$ in Fig. 3.4. However, while $\Delta n_c = +0.45$ is maximal for the thin films, for the thick films Δn_c can be further lowered by increasing α and w (see yellow dots in Fig. 3.7(a)), leading to values of the Modulation$/w$ (Fig. 3.7(b)) that are larger than the maximal value of 0.085 for the thin films (Fig. 3.5(b)). Here, the remarkable advantage of thick films comes about, since not only a larger thickness-normalized Modulation can be reached, the absolute Modulation values that can be generated are almost two orders of magnitude larger than these of the thin films (see the d_t-normalized Modulation in Fig. 3.7(b)).

3.4 Discussion and conclusion

We have developed a model that simulates travelling surface waves on azobenzene-modified liquid crystal polymeric systems triggered by a rotating polarized light source. Both thin films with intermediate light intensities and thick films with high intensities are presented that demonstrate the feasibility of creating peristaltic surface

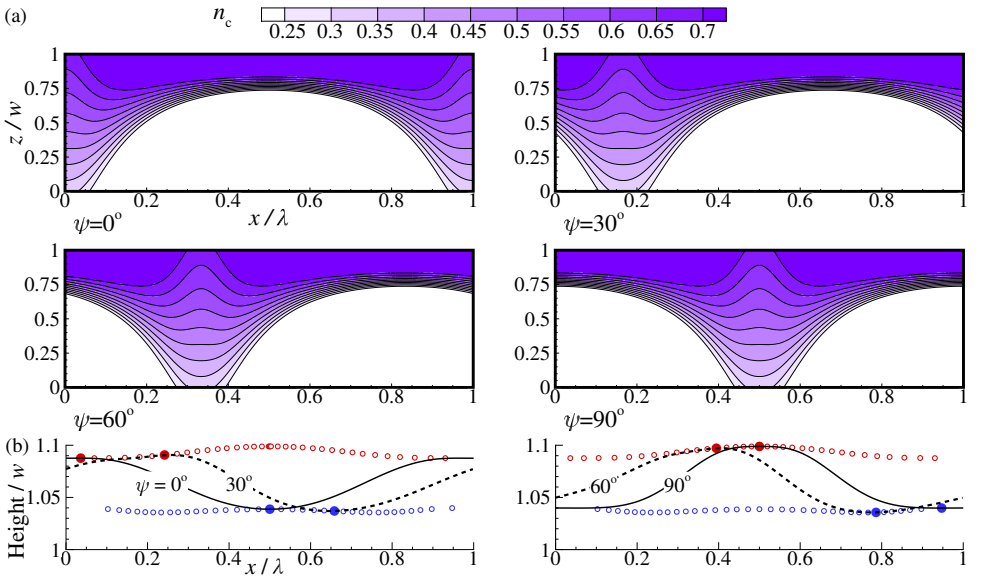

Figure 3.8 – *Evolution of the cis generation (a) and the surface profiles (b) under the rotating polarized light with $\psi = 0°$, 30°, 60° and 90° for a film with the thickness $w/d_t = 40$ and the light input $\alpha = 40$.*

motions, but with very different underlying photo-mechanical behaviour (compare Figs. 3.4 and 3.8).

For application in miniaturized microfluidic devices [331], our method is able to generate well-controlled, peristaltic waves with small Modulations on the order of 0.1 μm and wavelengths of several micrometers (take $d_t \approx 1$ μm for LC mixtures with 5-wt% azo-dosage [34] in combination with Fig. 3.5). On the other hand our system can also generate travelling wave with Modulations on the order of 10 μm (take $d_t \approx 1$ μm (ref [34]) in combination with Modulation/$d_t = 10$ for thick films in Fig. 3.7(b)). These Modulations that are a factor of 10 larger than in our previous work [34] and are comparable with other light-controlled liquid crystal elastomer systems [215]. Although it is not straightforward to make films with uniform directors through the depth of the film, considerable progress has recently been made in accurately controlling the director distribution in both thin [351] and thick [18] LC polymeric films. It should be noted that the absolute Modulation can be further enhanced by increasing the film thickness and light intensity (Fig. 3.7).

To estimate the speed of the travelling waves, we can use the actuation frequency from a recent experimental study using a similar material system [212], $f = 0.014 \cdot \mathrm{s}^{-1}$ (the light rotation speed is $2.5° \cdot \mathrm{s}^{-1}$), leading to a wave speed $U = \lambda f$ that scales with the wavelength λ, so that wave speeds of 0.11 $\mu\mathrm{m} \cdot \mathrm{s}^{-1}$ and larger can be obtained for films with $\lambda/w = 4$ and higher (cf. Fig. 3.4(b) taking $d_t = 1$ μm) or further higher for thick films. The swimming and propulsion speed, $V = 2\pi^2 A^2 f/\lambda$, can reach 1×10^{-2} $\mu\mathrm{m} \cdot \mathrm{s}^{-1}$ for thick films. It is slower than another LC elastomer swimmer [215] only due to the lower frequency. The wave speed can

be further enhanced by an increase in actuation frequency which has been observed for a glassy azobenzene-embedded LC polymer by a slight addition of visible light and temperature increase [212], attributed to a boosted *cis*-to-*trans* isomerization. Furthermore, a moderate addition of visible light is found to enhance the total light-induced strains due to the additional effect of continuous *trans*-*cis*-*trans* isomerization cycles [163, 175, 340], leading to wave amplitudes that can be a factor of 4 higher. Thus, we expect that the Modulation and frequency can be further enhanced leading to larger wave speeds and amplitudes and thus a higher flow efficiency for peristaltic microfluidic propulsion.

Exposing azobenzene-doped LC samples to high intensity light (required for the thick films, e.g., $\sim$ 1.1 W$\cdot$ cm^{-2} for $\alpha = 100$ in Fig. 3.7 according to the light parameter calibration in Ref. [34]) is reported to soften the material [294], which is not considered in the current work. To estimate the effect of photo-softening, we have performed additional simulations by accounting for a variation of the Young's modulus along the director, E_{11}, and perpendicular to it, E_{22}, by a factor that is larger than that experimentally reported (a reduction by a factor of 3 for UV intensity $I_0 = 300$ mW/cm^2 (ref [294])). Only a negligible difference was found compared with the non-softening results (See the supporting information of Ref. [213] for details).

The specific shape and speed of the surface waves can be controlled by the film thickness and light input. For intermediate film thicknesses, for which both positive and negative Δn_c can be reached by tuning the light intensity (cf. Fig. 3.3(c)), the amplitude of the wave can be controlled and even reduced to zero ($\Delta n_c \approx 0$), while keeping the rotation speed of the polarizer unaffected. In addition, the direction of the waves is guided by the rotation direction of the polarizer. Thus, the wave amplitude, wave speed and wave direction can be tuned through the light intensity, rotation speed and rotation direction of the polarized light source. This versatility allows application of this system for microfluidic propulsion in lab-on-chip devices [274, 352] , self-moving actuators [173, 215] and integrated soft robotics [325, 327, 353].

Acknowledgments

This research forms a part of the research programme of the Dutch Polymer Institute (DPI), project #775 TOPSWITCH. D.J. Broer acknowledges funding from the European Research Council under the European Union's Seventh Framework Programme (FP7/2007-2013)/ ERC grant agreement 669991. The authors would like to thanks Prof. Jaap den Toonder, Dr. Danqing Liu, Edwin De Jong and Matthew Hendrikx for useful discussions.

Appendix

3.A Rotatory travelling waves on disclination patterns

In this appendix, another type of travelling wave is designed and modeled based on disclination-type director patterns. Complex in-plane director patterning is possible via the help of photo-alignment layers. One special type of director manipulation is constructing high-order disclination styles of director distributions. Disclinations are widely observed in nematic liquid crystals [354–357], and usually are found with low strengths, e.g., half integers or ± 1 and randomly positioned [358].

A high-strength LC disclination profile can be created by imprinting pre-designed defects onto photo-alignment layers (see Fig. 3.9(a)). Then a liquid crystal nematic mixture is filled into the space between two pre-treated photo-alignment layers, and the LC molecules follow the imprinted style, which can be polymerized and frozen to preserve the strong rotation of the molecules even though it is energetically-unfavorable [147, 154, 201, 273, 359] (see Fig. 3.9(b)). The strength of a disclination/defect relies on the rotation speed ratio between the linear polarizer R_1 and the sample R_2 via the relation

$$m = 1 - R_1/R_2.$$

The director orientations surrounding the disclination core, which is a singularity point, can be described by its strength m in a polar coordinate reference frame (ρ, φ) as [264]

$$\theta = m\varphi + \theta_0,$$

where θ is the azimuth angle of the director (the tilt angle $\phi = 90°$) and θ_0 is an arbitrary starting reference angle. Some complex director patterns already achieved in experiments are shown in Fig. 3.9(c) and (d), with a maximal strength reaching ± 10 [273].

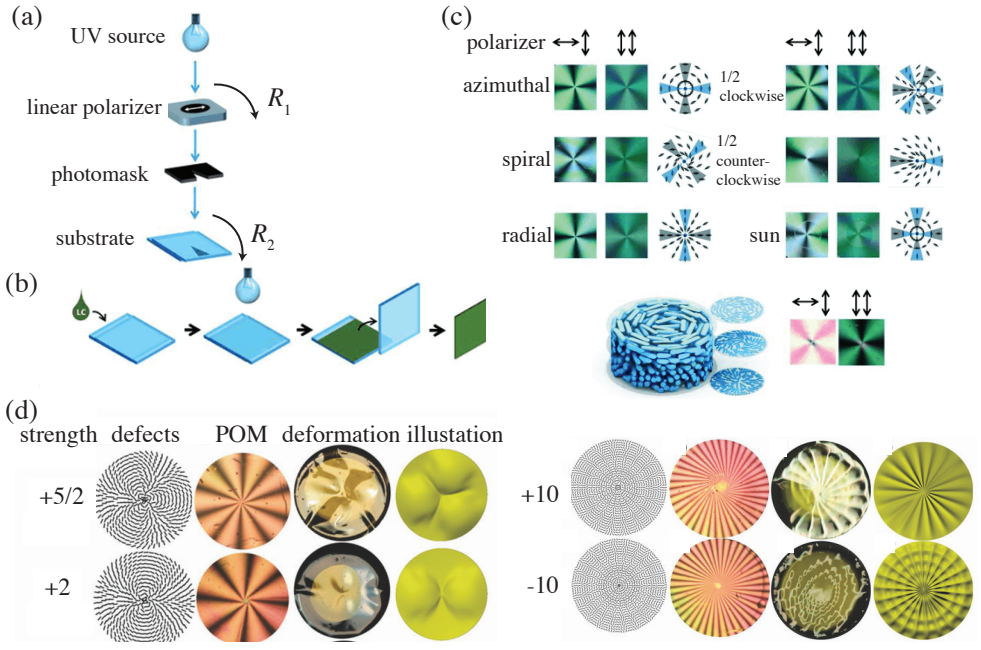

Figure 3.9 – *(a)-(b) Schematic of experimental procedures to fabricate disclination-like director patterns. (a) Photoalignment layers are first prepared via rotating a linear polarizer and a photoalignment substrate. The strength of the defect relies on the rotation speeds ratio between R_1 and R_2, $m = 1 - R_1/R_2$. (b) Next a LC mixture is filled between two photoalignment layers and the director profile is frozen after polymerization. (c) Images of several samples under cross polarizers with schematics of the director distribution. (d) Exemplary films with high-strength disclination director patterns and the corresponding images under crossed polarizes, as well as the deformations under diffuse light actuation. (Figures (a)-(c) reproduced from Ref. [154], (d) from Ref. [273], copyright Wiley).*

The mechanism developed in Chapter 3 for the polarized-light-guided topographical manipulation is extended here. The simulation results are presented in Fig. 3.10. The input parameters used in Section 3.3.2 are adopted here. The boundary conditions at all the lateral surfaces of the test films are traction free (in contrast to the periodic boundary condition used for the film in Sections 3.3.2-3.3.3).

With such complex in-plane director patterns, alternating patterns of ridges and valleys are generated, see figure 3.10. The number of the ridges (and the valleys) is equal to $2 \times |m|$, e.g., four and sixteen ridges ensue for the cases with $m = \pm 2$ and ± 8, respectively. Upon a rotating polarized light source, the textures also rotate, mimicking angular travelling waves, or a rotating "Roulette". The rotation direction is the same as that of the polarized input light for disclinations $m > 0$, and opposite for $m < 0$ (see the difference in profile changes for $m = 2$ and -2 in Fig. 3.10).

The magnitude of the out-of-plane deformations varies with the disclination strength. With smaller m, the ridges and valleys can deform more due to the lower mechan-

ical constraints from the neighboring regions. Some edge effects occur at the free boundaries.

The results presented in this appendix serve as an example of manipulating surface textures by designing complex in-plane director patterns and achieving peculiar topographical changes. Possible applications of this angularly-travelling wave might include fluid mixing in micro-mixers and self-rotating or propelling of micro-actuators or nano-motors [215, 360, 361], micro-resonators [362] and biological tissue mimic [363].

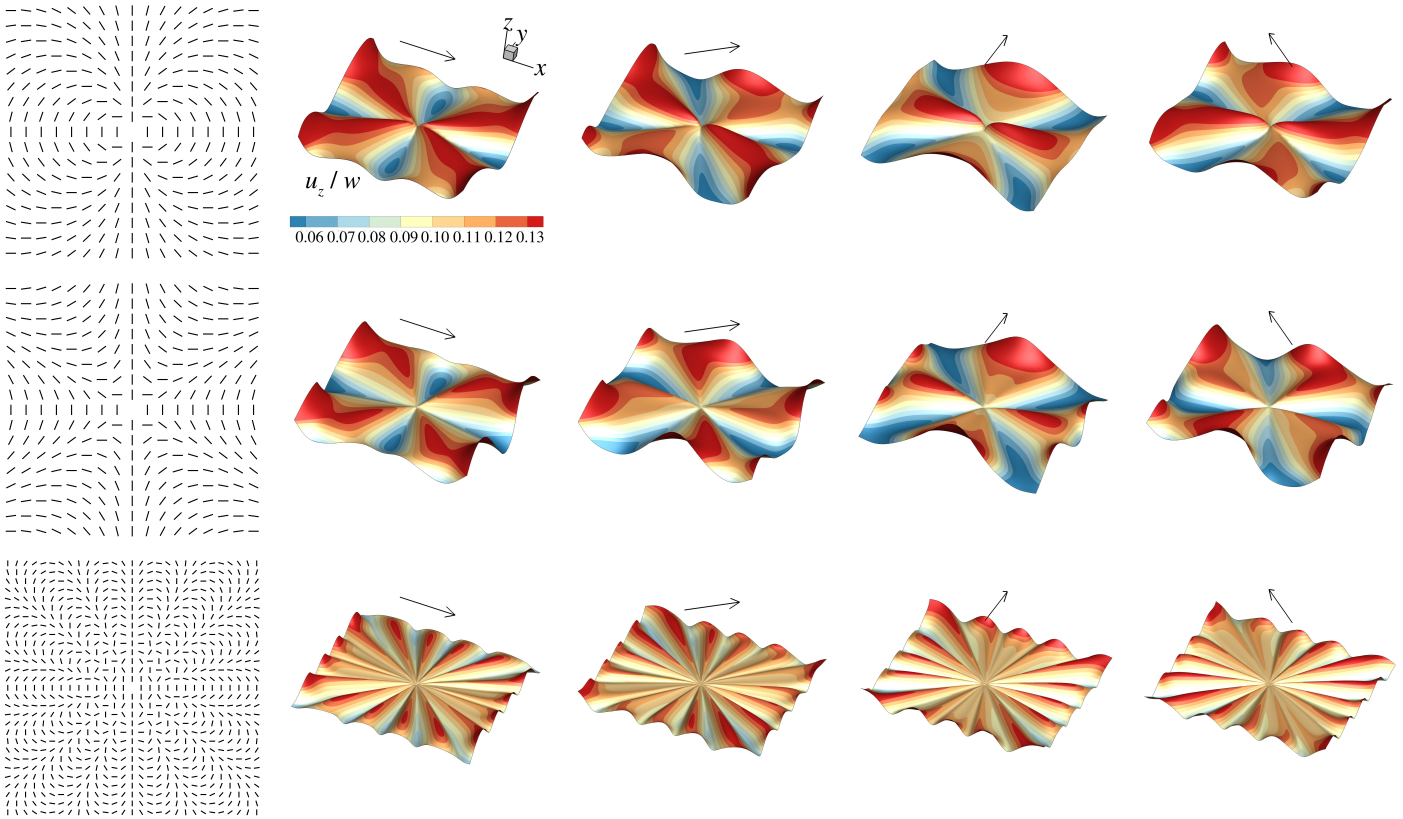

Figure 3.10 – *Schematic (leftmost) and 3D topographies of films having disclinations with strength $m = 2$ (upper row), -2 (middle row) and 8 (bottom row) superimposed by contour plots of normalized out-of-plane displacement u_z/w. The rotating polarized light is indicated by the arrow (the light polarization directions from left to right are 0°, 45°, 90° and 135° with respect to the x-axis, respectively). The travelling topographies mimic a rotating "Roulette".*